2021

SUPER-RESOLUTION IMAGING OF REMOTE SENSED BRIGHTNESS TEMPERATURE USING A CONVOLUTIONAL NEURAL NETWORK

Kellen A. Donahue

SUPER-RESOLUTION IMAGING OF REMOTE SENSED BRIGHTNESS

TEMPERATURE USING A CONVOLUTIONAL NEURAL NETWORK

By

Kellen A. Donahue

Bachelor of Arts in Mathematics, University of Montana, Missoula, Montana, 2017
Bachelor of Arts in Physics, University of Montana, Missoula, Montana, 2017

Thesis

presented in partial fulfillment of the requirements
for the degree of

Master of Science
in Computer Science

The University of Montana
Missoula, MT

June 2021

Approved by:

Scott Whittenburg, Dean of The Graduate School
Graduate School

Jesse Johnson, Chair
Computer Science

Doug Brinkerhoff
Computer Science

John S. Kimball
Systems Ecology

Donahue, Kellen, M.S., Spring 2021   Computer Science

Super-resolution Imaging of Remote Sensed Brightness Temperature Using a Convolutional Neural Network

Chairperson: Jesse Johnson

Steady improvements to the instruments used in remote sensing has led to much higher resolution data, often contemporaneous with lower resolution instruments that continue to collect data. There is a clear opportunity to reconcile recent high resolution satellite data with the lower resolution data of the past. Super-resolution (SR) imaging is a technique that increases the spatial resolution of image data by training statistical methods on simultaneously occurring lower and higher resolution data sets. The special sensor microwave/imager (SSMI) and advanced microwave scanning radiometer (AMSR2) brightness temperature data products are well suited to super-resolution imaging, and SR can be used to standardize the higher resolution across the entire record of observations. Of the methods used in super-resolution imaging, neural networks have led to major improvements in the realm of computer vision and have seen great success in the super-resolution of photographic images. We trained two neural networks, based on the design of the Resnet, to super-resolution the 25 kilometer resolution SSMI and AMSR2 brightness temperature data products up to a 10 kilometer resolution. The mean error over all frequencies and polarizations for the AMSR and SSMI models' predictions is 0.84% and 2.4% respectively for the years 2013 and 2019.

1. Introduction

Remote sensing data provides critical information for weather forecasting, resource management, conservation, and exploration over comprehensive spatial and daily temporal scales. Remote sensed data products have many uses including crop freeze injury [1,2],landslide detection [3], and forest monitoring[4,5]. The 34 year time series, daily acquisition, sensitivity to the state of water[6], and global reach of the brightness temperature products makes them useful for applications such as monitoring soil freeze thaw cycles[6], soil moisture[7,8], and cloud dynamics[9,10]. As is often the case, higher resolution and extended coverage improve the effectiveness of these data products for complex terrain[11],resource assessment, and operational planning[12]. Modern brightness temperature products offer increased resolution, but their temporal coverage only extends back to 2012, whereas lower resolution products begin coverage in 1987. As it currently stands, any analysis carried out on these data must be tailored to either the higher resolution of modern products or the lower resolution, but longer period of observation found in the older data products. In order to 'harmonize' data products for analysis, we propose to upscale lower resolution data to the same resolution as recent, higher resolution products, extending high resolution data through the entire observational period.

Super-resolution imaging (SR) is the technique of upscaling low resolution imagery to higher resolutions. There are well known methods for achieving this such as bicubic interpolation, spline approximation, and kriging[13]. SR is often applied to photographic images and has seen application in video enhancement, surveillance, medical diagnosis, and biometric identification[14]. As with many computer vision tasks, recent years have demonstrated that neural networks produce impressive improvements to SR. Neural networks have achieved increased resolutions of up to 50 times on photographic imagery[15,16],satellite imagery[17–19], and global climate model data[12].

Brightness temperature products span various resolutions and radiometer frequencies. The SSMI brightness temperature product extends back from today to 1987 at 25 km resolution for the 19.35, 22.24, 37.0, and 85.5 GHz frequencies and both vertical and horizontal polarizations except for 22.24 GHz which lacks a horizontal polarization. Alternatively, the AMSR2 brightness temperature product only extends back to 2012, has both 25 km and 10 km resolutions, and is observed at 7.3, 10.65, 18.7, 23.8, 36.5, and 89.0 GHz frequencies in both vertical and horizontal polarizations. The similar frequency and overlap in coverage between the SSMI 19.35 and 37.0 GHz with the AMSR 18.7 and 36.5 GHz channels respectively, makes these frequencies our focus as inputs in training our neural network.

In the following sections we present the use of a CNN to SR brightness temperature data. In section 2, we describe training a convolutional neural network to SR the 25 km AMSR2 brightness temperature data up to the 10 km resolution. This task is straightforward as we SR data from the same sensor at different resolutions. We then train a second network to SR 25 kilometer SSMI brightness temperature data to a 10 km resolution on the AMSR2 grid, again using the AMSR2 10 km resolution data for training. This SSMI to 10 km network provides the means of creating a harmonized data product that reconciles both SSMI and AMSR2 data to the same 10 km grid. Finally, we train a third network to SR 90x90 patches of 25 km AMSR2 up to 10 km resolutions that can be reconstructed into a global grid. This network has the advantage of

3

being able to be applied to 90x90 patches of data from different projections. In section 3, we report the performance metrics of our networks and break them down by land cover type for one of our networks. Finally in section 4, we discuss the limitations of our approach as well as the major error sources seen in the results and comment on the computational performance of our networks.

2 - Method

2.1 - Experiment design

We use the AMSR2 10km and 25km standard products from JAXA[20] and the Pathfinder Daily EASE-Grid 25km SSMI data[21]. To upscale the 25km brightness temperature data to a higher 10km resolution we developed a CNN based neural network and trained three independent networks for the task. First, we first trained a network that takes global 25km AMSR2 brightness temperature data as an input and produces a 10km output to be compared with the actual 10km AMSR2 data. This network is useful as a measure of the network's performance when doing SR between datasets with exactly matching acquisition times and frequencies. In this paper, this will be referred to as the SR AMSR network. The second network we trained to SR 25 km SSMI data to the same 10km resolution used in the first network. For training purposes, this network's output is also compared against 10km AMSR2 data. This network will gauge whether the network can learn SR from the different datasets and will be referred to as the SR SSMI network. It's worth pointing out that we had intended to train the SR AMSR and then perform transfer learning to generate the SR SSMI network. Although this approach worked,we achieved the same results by fully training the SR SSMI network without transfer learning in less time, which was useful when experimenting with the model. The third network will be trained differently than the other two. The 25km AMSR data will be tiled and the network will SR each tile individually before they are reconstructed into the full global 10km grid. When training the network it will only be trained on the northern hemisphere to show its ability to predict the southern hemisphere without having been trained on it. This is useful because there is at least partial spatial memorization involved in the other networks so this network acts as a test of the network's performance without that memorization. This network will be referred to as the SR Tile network.

To create the SSMI data for the SR SSMI network we first interpolate the SSMI data from the 25km EASE-GRID to the 25km equirectangular projection of AMSR2 using a degree 3 bivariate spline over a rectangular mesh (RBS). One problem with this approach is that pixels around missing data swathes are interpolated between actual data and the missing data value of 0, giving erroneous values. To correct this we used a degree 1 RBS interpolation of the missing swathes of data and then dilated the result by 1 pixel creating a mask to replace the values near the missing swathes.
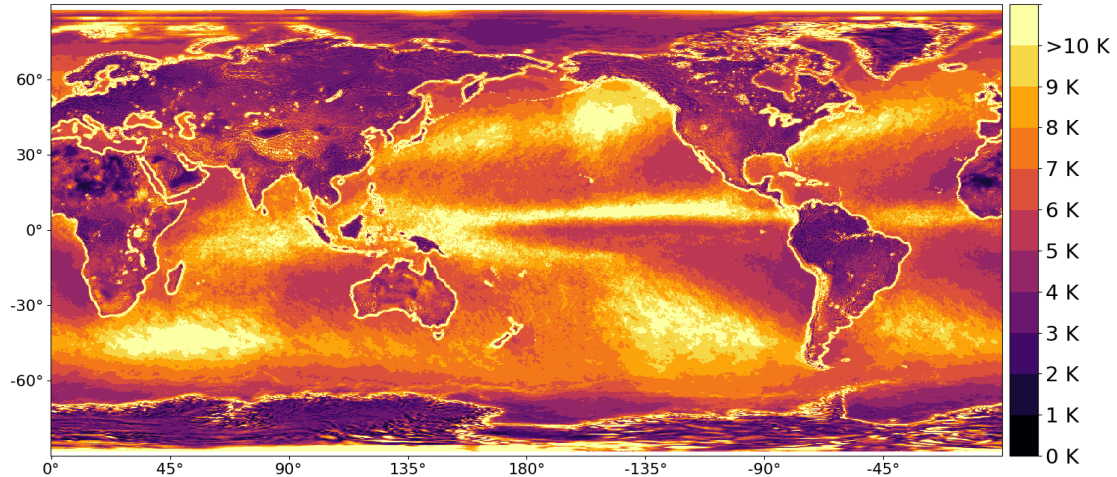
Figure 1. Averaged absolute difference heatmap between the 18.7 vs 19.35 GHz and 36.5 vs 37 GHz channels for the year 2013

2.2 - Systematic Errors

Figure 1 shows an absolute difference heatmap between similar frequencies of the 25km SSMI and 25km AMSR. Differences between the data products are expected due to their different acquisition times, sensor calibrations, and frequencies. The equatorial crossing time for AMSR2 is 1:30 pm on the ascending pass and 1:30 am on the descending pass, and for SSMI, the ascending equatorial pass is 6:30 pm and the descending pass is 6:30pm[22]. The mean absolute and percent errors between the two products globally are 6.69°K and 3.57% respectively. However, most of the errors are generated in the ocean and arid and coastal land regions. The low differences of roughly 2-5°K on land and some sea surfaces gives us confidence in the combination of these two data products for training neural networks, with a few caveats. Larger errors on coastlines are likely due in part to reprojecting 25km SSMI to the 25km AMSR grid because large differences between land and ocean brightness temperature readings are interpolated into single grid cells. Furthermore, pixels containing as little as 4% open water can bias readings by over 3°K[23] which will affect the brightness temperature readings near shorelines. Precipitating cloud coverage plays a role in error due to change in cloud position between readings as these cloud covered regions appear warmer compared to the ocean at these frequencies[24]. For land, the precipitation will impact soil moisture which has a large effect on surface emissivity and therefore recorded brightness temperatures[23]. The large differences in hot arid land regions are likely due to the large diurnal temperature variance in these regions[25]. Partial coverage of sea-ice will lead to high variation in ocean brightness temperatures due to emissivity differences[26]. Similarly, snow, frost, and frozen soil affect brightness temperature readings leading to variation in higher latitude regions[6]. We will use the error layout of figure 1 to help gauge the performance of our SSMI SR outputs.

5

2.3 - Model

Our model only uses a single band and polarization at a time as an input. We experimented with feeding the network different combinations of bands and polarizations but they all performed worse than the single band approach. Furthermore, we experimented with the addition of other data sources such as a digital elevation mask, snow cover, and vegetation type. These also led to equal or worse performance to just using brightness temperature.
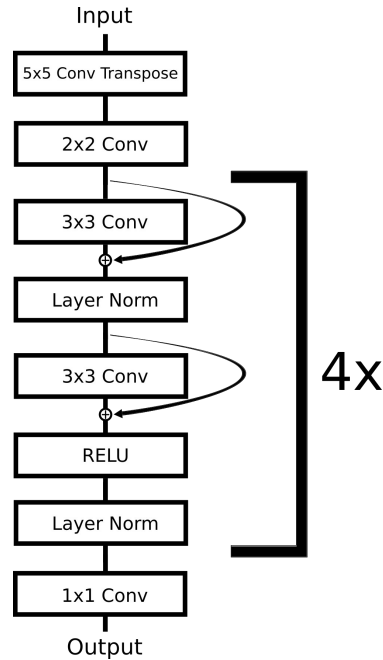
Input

5x5 Conv Transpose

2x2 Conv

3x3 Conv

Layer Norm

3x3 Conv

RELU

Layer Norm

4x

1x1 Conv

Output

Figure 2. Architecture of our CNN

SR of the 25 km products to the 10 km resolution requires the upscaling of 720x1440 inputs to an 1800x3600 output, or a size increase of 6.25 times. We used a transposed convolution with a 5x5 kernel and 5x5 stride to scale our input by 25 times and then use a convolution with a 2x2 kernel and 2x2 stride to reduce it by 4 times which results in a change of 6.25 times from the input. Afterward, the network follows a resnet[27] inspired design. Each block contains a convolutional layer followed by an additive skip connection and a layer normalization[28] repeated twice with a ReLU activation inserted before the second layer normalization. This block is repeated 8 times then followed by a 1x1 convolution to produce the output. Layer normalization requires consistent input shape which limits the network to a single input size. Therefore, SR Tile is made to work on 90x90 inputs while SR AMSR and SR SSMI are made to work on 720x1440 inputs. When reconstructing the full image with outputs from SR Tile there are artifacts along the edges of the tiles due to slight mismatch between model output on tile edges. To fix this we pad the input by 40 pixels on all sides before tiling and make 5 outputs by shifting the tiling window by 20 pixels vertically and horizontally each

time. These 5 outputs are then aligned and averaged to remove the edge artifacts.

Though the network is simple, it proved to be effective with only 4 channels which was essential when working with the high resolution images to run the network within available memory. The models were trained on four Nvidia V100 GPUs using Adam[29] with an initial learning rate of 1e-2 that was manually reduced by factors of 2 between iterations once training slowed down. All networks were trained on data from 2014 through 2018 and then tested on 2013 and 2019 data.
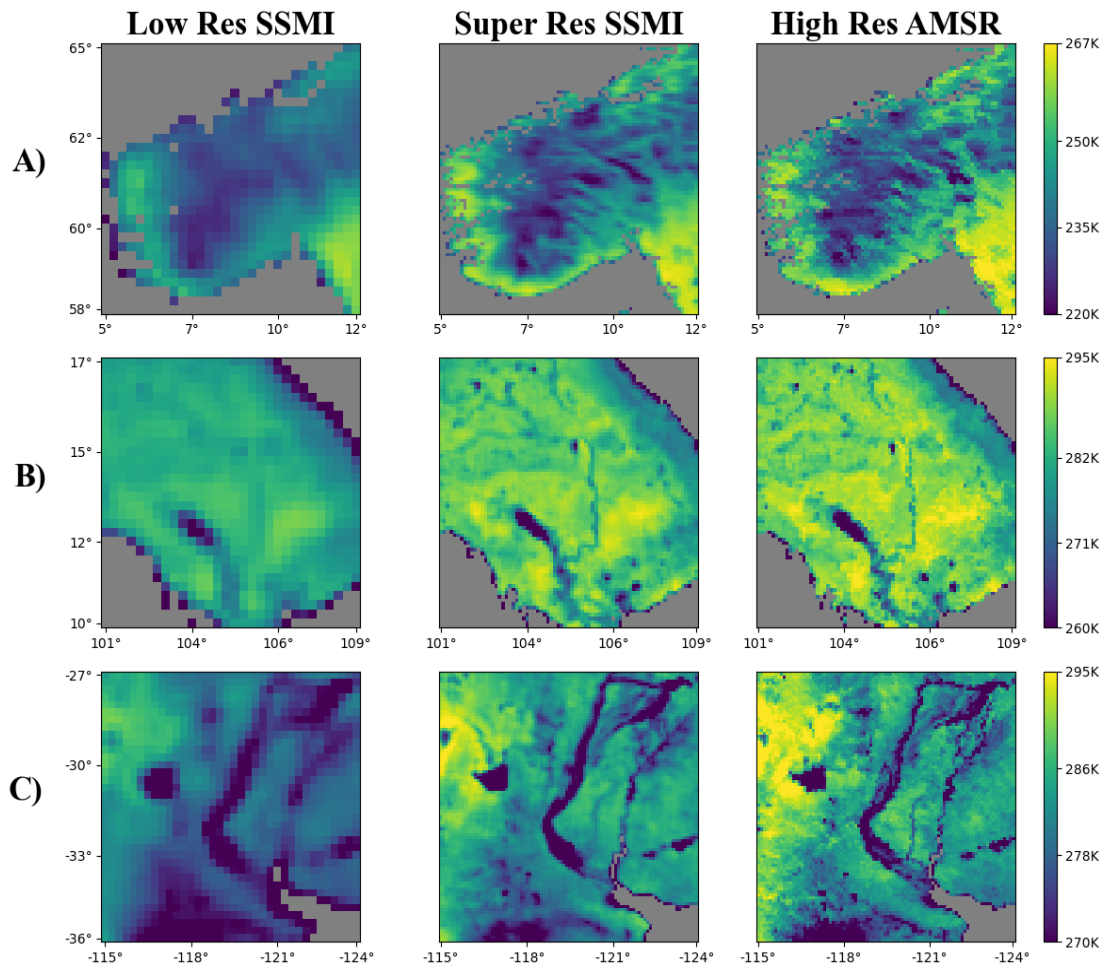
Figure 3. Comparison of LR SSMI, SR SSMI, and HR AMSR 37 GHz vertical polarization data for 2013-01-01. Shown are: (A) Norwegian Peninsula; (B) Indochinese Peninsula; (C) Region around the Rio De La Plata. The ocean has been masked in gray to accentuate the details in brightness temperature found on land.

3. Results

The results of the SR procedure are presented for selected sub-regions in Figure 3. The left and right columns contain actual brightness temperature readings while the middle column is the SR output of our SR SSMI model. Differences between the center column and the left column represent the 'information' that is filled in by the SR SSMI model. Differences between the middle and right columns will be a combination of model errors and as seen in Fig. 1; differences between the frequency, timing, and sensors of the products. Our results suggest the model is successfully reproducing a great deal of the fine scale structure missing in the 25 km resolution data, though it does have a smoothed appearance that is typical to SR by CNNs[19].

Commonly used approaches to resolution enhancement of brightness temperature include Backus-Gilbert Interpolation and Signal Reconstruction Algorithms[30,31]. These approaches work on the ungridded satellite swath data to produce high resolution gridded products. This is different from our approach which works on the already gridded low resolution products to produce a higher resolution product. As such comparison between these techniques and ours is tenuous. Instead, we compare our product's performance against two different SR techniques. The first is simple bicubic interpolation for a baseline as is common for SR[12,16,18,19]. But, bicubic interpolation will inherently smooth out high frequency data and so for a second comparator we use a modified bicubic interpolation technique that takes advantage of the static nature of the data's global grid. We first find the mean difference between bicubic interpolated data and the 10km AMSR2 data over the course of a year. We then subtract this mean difference from the bicubic interpolated data in order to return some of the high frequency detail that is lost with basic bicubic interpolation. This technique will be referred to as Mean Bicubic Interpolation(MBI). MBI will not be applied to SSMI data as it doesn't make sense to do this for differing datasets. Our metrics include mean per-pixel absolute error(MAE), mean per-pixel percent error(MPE), Structural Similarity (SSIM) and Peak Signal-to-Noise Ratio (PSNR). SSIM is of particular interest due to its consideration of structural information of the image[32].

8

Table 1. 2013 and 2019 performance metrics for our three models as well as bicubic interpolation and MBI.

Model	MAE	MPE	SSIM	PSNR
SR AMSR	1.65	0.82	0.949	38.01
SR Tile	1.77	0.90	0.946	36.17
SR SSMI	4.47	2.40	0.887	29.34
Bicubic AMSR	2.75	1.40	0.917	29.93
MBI AMSR	2.13	1.07	0.929	31.73
Bicubic SSMI	9.37	4.86	0.831	19.85

Table 1 compares our networks against bicubic interpolation and MBI. We can see that MBI produces notable improvements over basic bicubic interpolation and thus acts as a more effective baseline of comparison. The SR AMSR network outperforms MBI by 0.45°K for MAE, 0.21% for MPE, 0.05 for SSIM, and 2.01 for PSNR. Likewise, SR SSMI sees improvements over bicubic interpolation of 4.9°K, 2.46%, 0.06, and 9.49 for MAE, MPE, SSIM, and PSNR respectively. Table 1 contains the global results for SR Tile and shows that it underperforms SR AMSR but is still ahead of bicubic interpolation and MBI. For just the southern hemisphere, SR Tile achieves 1.58°K, 0.85%, 0.959, and 37.51 for MAE, MPE, SSIM, and PSNR respectively, demonstrating SR Tile's ability to work on unseen geographic locations.

Table 2. Mean Percent Error for each polarization and frequency of SR AMSR and SR SSMI by land cover type. Categories are: A)Artificial Surfaces, B) Cropland, C) GrassLand, D) Tree Covered, E) Shrub Covered, F) Herbaceous vegetation, G) Mangroves, H) Sparse Vegetation, I) BareSoil, J) Snow and Glaciers, K) Water Bodies, L) General Land

Model	Frequency	Polarization	A	B	C	D	E	F	G	H	I	J	K	L
SR AMSR	37 Ghz	Vertical	0.94	0.62	0.63	0.59	0.65	0.43	2.05	0.64	0.59	0.50	0.69	0.57
		Horizontal	1.69	0.84	0.84	0.80	0.86	1.17	4.28	0.89	0.74	0.67	1.45	0.77
	18 Ghz	Vertical	0.91	0.51	0.46	0.46	0.50	0.58	1.91	0.48	0.46	0.42	0.61	0.46
		Horizontal	1.54	0.79	0.66	0.68	0.75	0.96	3.91	0.73	0.63	0.49	1.14	0.63
SR SSMI	37 Ghz	Vertical	2.09	1.83	2.28	1.93	1.81	2.97	2.08	2.33	1.48	1.83	2.73	1.92
		Horizontal	3.17	2.27	2.73	2.29	2.16	3.83	4.00	2.87	1.78	2.34	5.50	2.36
	19 Ghz	Vertical	2.02	1.50	1.60	1.47	1.41	2.12	1.98	1.65	1.20	1.43	2.21	1.47
		Horizontal	3.07	2.08	2.20	1.89	1.86	3.09	3.68	2.41	1.63	1.92	4.07	1.98

To further assess the quality of our SR AMSR and SR SSMI networks we look at the mean percent error for different land cover types provided by the Global Land Cover Share Database(GLCS)[33] and present the results in Table 2. We use the dominant land cover type of a pixel to determine its category and take a mean of all similarly classed pixels to determine their score. GLCS does not include Antarctica so we added it under the classification of snow and

glaciers. Additionally, we include a column for land as a whole to present the model's general performance on land. Land is determined to be all pixels not classified as water bodies. We also report the results for each polarization individually due to the large disparity between polarizations for most categories. Table 2 shows that SR AMSR performs well in all regions except for mangroves, possibly due to mangroves being on coasts where brightness temperatures are highly variable. As for SR SSMI, it performs best in cropland, grassland, and tree covered regions. On the other hand it performs worse in snowy or moist land regions.

4. Discussion

In this work we implemented a CNN to SR 25km brightness temperature data up to a 10km resolution. Due to our novel approach we are unable to compare against an existing product. Instead, the outputs of the network are compared against bicubic interpolation methods using percent error, SSIM, and PSNR as metrics. Our SR AMSR model achieved a percent error of .84% compared to bicubic interpolations 1.4%. Even better, our SR SSMI model achieved a percent error of 2.4% compared to bicubic interpolations 4.86%.
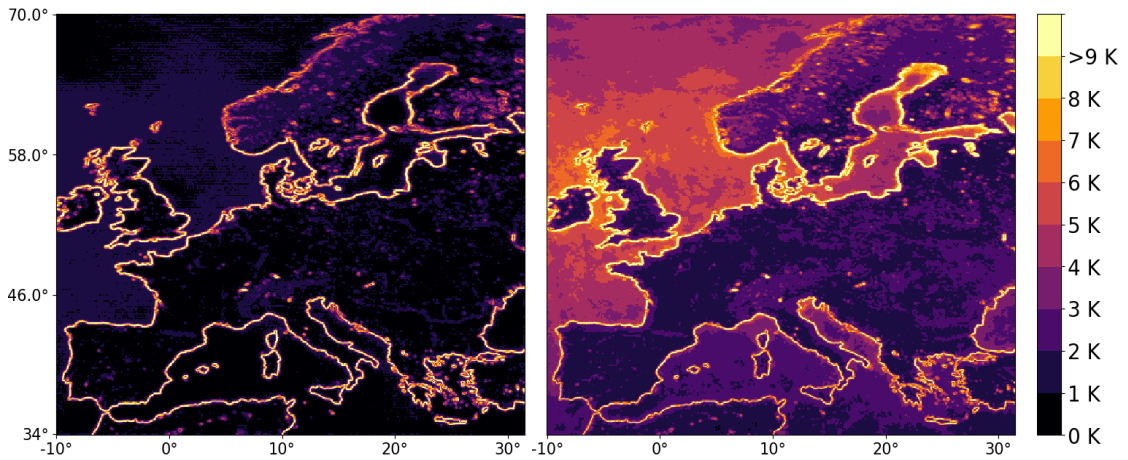

Figure 4. SR AMSR(left) and SR SSMI(right) absolute error heatmaps of Europe for all frequencies and polarizations.

Figure 3 contains a mean absolute error heatmap for our SR AMSR and SR SSMI networks over Europe. Europe is chosen due to its wide range of environments while allowing a more detailed view compared to a global map. When analyzing the error in the SR AMSR data we can see some problem areas. The Coastlines have a consistently high level of error for both inland water bodies and oceans. Furthermore, water bodies have higher error levels compared to the land. High elevation

10

mountain ranges such as the alps or the scandinavian mountains tend to also have higher amounts of error.

For SR SSMI, similar to SR AMSR, we can see errors in shorelines, mountains, and the ocean but with higher magnitudes as expected from the differences between the SSMI and AMSR datasets. When comparing the errors to the low resolution errors in figure 1 we can see that the network maintains errors in similar regions though there is an overall decrease in error of roughly 2°K. A weakness in our approach is the use of different brightness temperature data products to train our network. Though our datasets are of similar bands and inspection of our SR data shows realistic results, this doesn't change that our network is trying to infer between two different data products. We can provide potential explanations for major error regions, but the weakness of the approach is that we can't be sure if an error is because of a prediction problem or because of a difference in datasets.
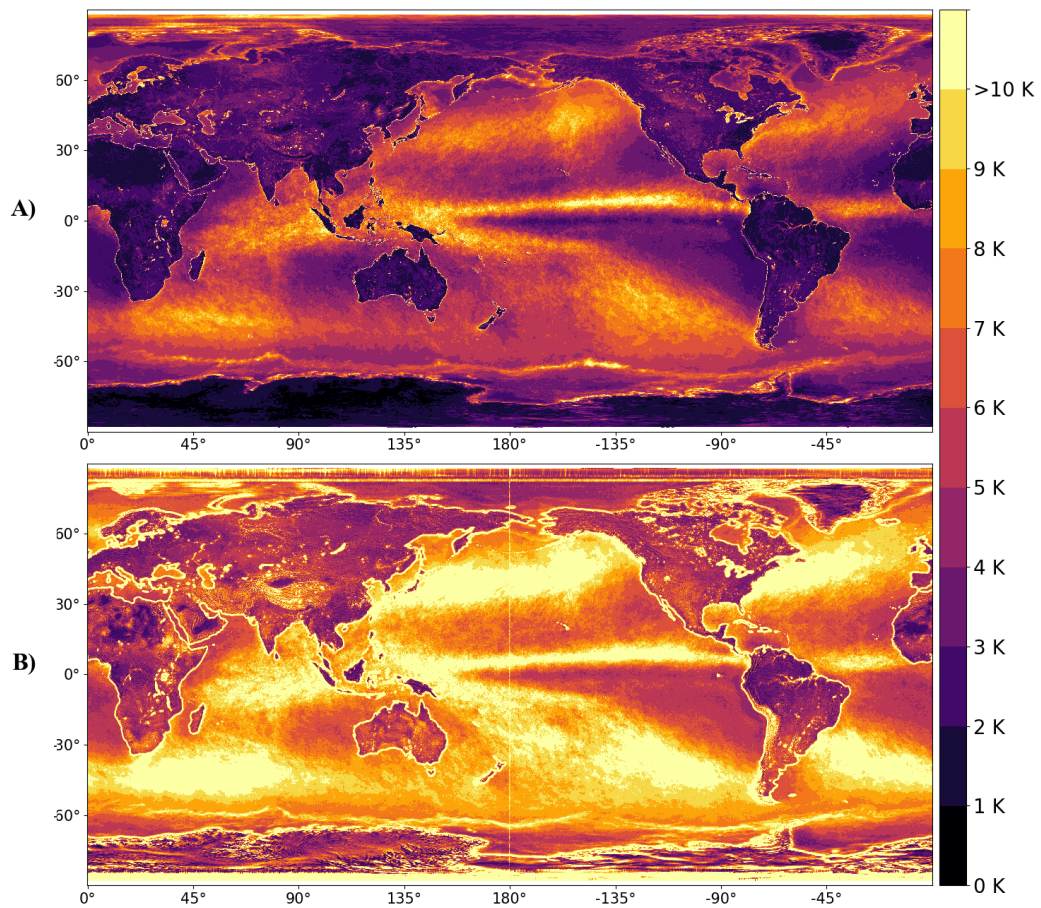
Figure 5. Averaged absolute difference heatmap of the 18.7 vs 19.35 GHz and 36.5 vs 37 GHz for A) SR SSMI vs 10km AMSR and B) SR Tile on SSMI vs 10km AMSR.

Figure 5 shows an absolute difference heatmap between similar frequencies of the SR SSMI and reprojected SR Tile vs 10km AMSR, similar to figure 1 for the low resolution data. Because SR Tile works on 90x90 patches it can be applied to SSMI data without reprojection. This has the advantage of avoiding reprojection errors but seems to cause an artifact along the 180° longitude line, possibly due to SSMI's width of 1383 being reprojected 2.5x to 3457.5. We can see that both heatmaps maintain the distribution of differences seen in figure 1, but the magnitude of the differences have changed. The differences in SR SSMI have decreased by roughly 3-5°K. This suggests that the network is trying to SR the SSMI data it is given, but its output values have drifted closer to AMSR values. Alternatively, SR Tile sees an increase in error of 1-3°K in some places, but overall the magnitude of the errors are much closer to those seen in the low resolution data. For 25km SSMI and AMSR data the MAE is 6.69°K and MPE is 3.57%. As expected from figure 5, SR SSMI achieves an MAE of 4.47 and MPE of 2.40%, which are both lower than the 25km values. Finally, SR Tile has an MAE and MPE of 7.64°K and 3.72% respectively, much closer to the 25km values than SR SSMI. This suggests that SR Tile is a better approach to SR data that doesn't have a corresponding high resolution dataset to train the network with.

12
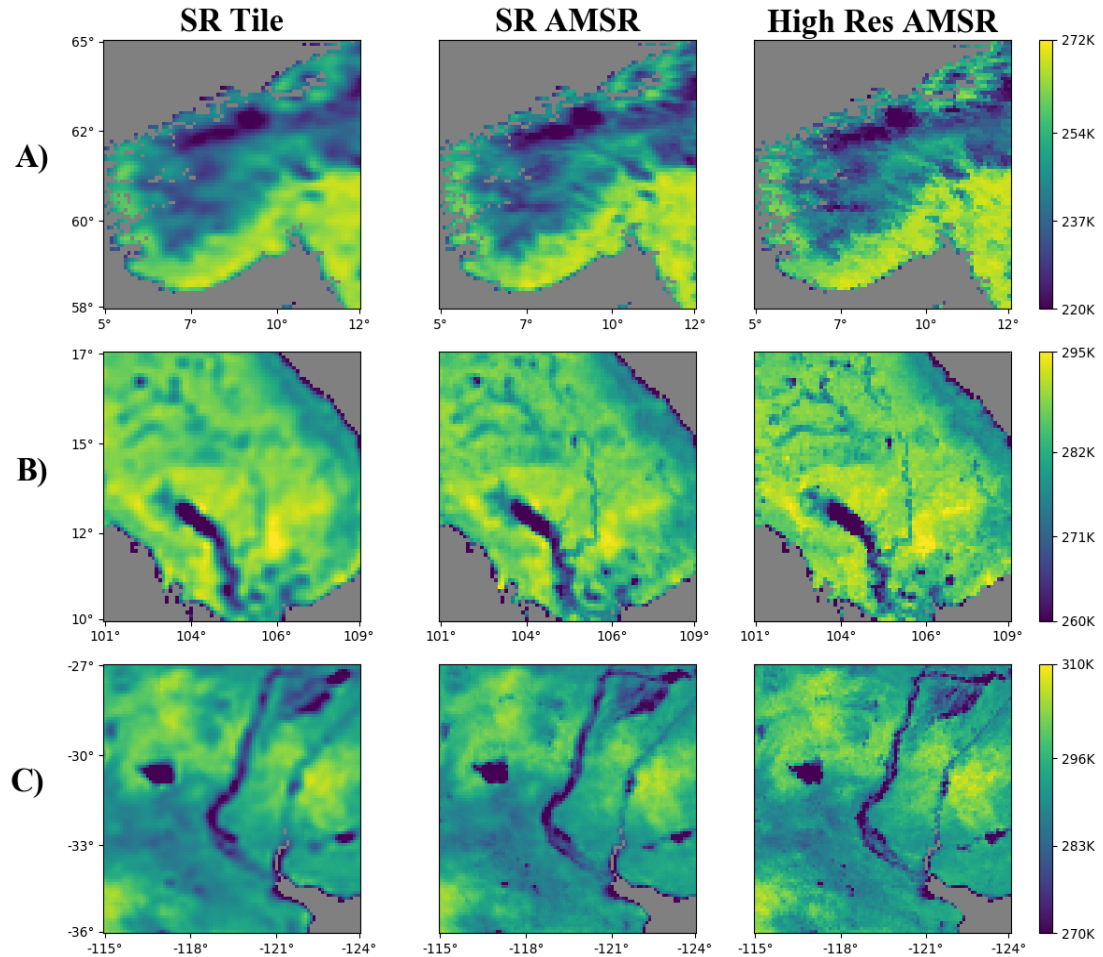
Figure 6. Comparison of SR Tile, SR AMSR, and HR AMSR 37 GHz vertical polarization data for 2014-01-04. Shown are: (A) Norwegian Peninsula; (B) Indochinese Peninsula; (C) Region around the Rio De La Plata. Again, The ocean has been masked in gray to accentuate the details in brightness temperature found on land.

The trade-off for using a tiling approach is a loss of refined detail compared to the global SR models. Figure 6 shows a comparison between SR Tile, SR AMSR and actual 10km AMSR2 data. Comparing SR Tile and SR AMSR we can see that SR AMSR manages to capture finer details of the actual 10km data. Though memorization is often avoided in machine learning, this shows the advantage of the network being able to memorize spatial details by working on a global grid. The impact of the loss of generalizability is minimized as the network is designed to only work on global AMSR data. The risk is that should a major geographic change take place, like the creation or draining of a man-made lake, the network will likely struggle to adapt so it will need to be trained on new data to avoid this.

13

The different brightness temperature polarizations perform quite differently from each other. As seen in table 2 the horizontal polarizations perform much worse than their vertical counterparts in all regions. This can be at least partially attributed to the higher sensitivity of horizontal polarizations to moisture[23]. For SR SSMI, the time difference between the two datasets would lead to even greater variation due to the compounded effect of moisture change between readings. This higher error may be unavoidable due to the aforementioned reasons, but it could perhaps be improved by creating specialized networks for each different polarization to allow the network to focus on the specific connections between each polarization.

Further improvements could be made by the use of additional or different datasets that have closer relationships. Use of the SSMI and AMSR2 quality control flags could be useful for masking out things like cloud, sea ice, and radio frequency interference. Another potential improvement would be the use of a loss function such as SSIM which utilizes the structural information provided by the AMSR data with less focus on the exact values, though in our tests SSIM was too unstable and resulted in NaN values during training. Additionally, testing different neural network models such as SRGANS[15] that have shown promising results in other SR tasks could be useful, though memory requirements may make this difficult for a non-tiled approach.

References

1. Feng, M.-C.; Yang, W.; Cao, L.-L.; Ding, G.-W. Monitoring Winter Wheat Freeze Injury Using Multi-Temporal MODIS Data. *Agric. Sci. China* **2009**, *8,* 1053–1062.
2. She, B.; Huang, J.-F.; Guo, R.-F.; Wang, H.-B.; Wang, J. Assessing Winter Oilseed Rape Freeze Injury Based on Chinese HJ Remote Sensing Data. *J. Zhejiang Univ. Sci. B* **2015**, *16,* 131–144.
3. Zhao, C.; Lu, Z. Remote Sensing of Landslides—A Review. *Remote Sensing* **2018**, *10,* 279.
4. Coops, N.C. Characterizing Forest Growth and Productivity Using Remotely Sensed Data. *Current Forestry Reports* **2015**, *1,* 195–205.
5. Wang, L.; Jia, M.; Yin, D.; Tian, J. A Review of Remote Sensing for Mangrove Forests: 1956–2018. *Remote Sens. Environ.* **2019**, *231,* 111223.
6. Kim, Y.; Kimball, J.S.; Glassy, J.; Du, J. An Extended Global Earth System Data Record on Daily Landscape Freeze–thaw Status Determined from Satellite Passive Microwave Remote Sensing. *Earth Syst. Sci. Data* **2017**, *9,* 133–147.

7.   Chen, W.; Shen, H.; Huang, C.; Li, X. Improving Soil Moisture Estimation with a Dual Ensemble Kalman Smoother by Jointly Assimilating AMSR-E Brightness Temperature and MODIS LST. *Remote Sensing* **2017**, *9*, 273.

8.   O'Neill, P.; Entekhabi, D.; Njoku, E.; Kellogg, K. The NASA Soil Moisture Active Passive (SMAP) Mission: Overview. In Proceedings of the 2010 IEEE International Geoscience and Remote Sensing Symposium; July 2010; pp. 3236–3239.

9.   Wang, C.-C.; Chen, G.T.-J.; Carbone, R.E. A Climatology of Warm-Season Cloud Patterns over East Asia Based on GMS Infrared Brightness Temperature Observations. *Mon. Weather Rev.* **2004**, *132*, 1606–1629.

10.   Stephens, G.L.; Kummerow, C.D. The Remote Sensing of Clouds and Precipitation from Space: A Review. *J. Atmos. Sci.* **2007**, *64*, 3742–3765.

11.   Kim, Y.; Kimball, J.S.; Du, J. Satellite Microwave Remote Sensing of Landscape Freeze--Thaw Status Related to Frost Hazard Monitoring. In *Remote Sensing of Hydrometeorological Hazards*; CRC Press, 2017; pp. 157–182.

12.   Stengel, K.; Glaws, A.; Hettinger, D.; King, R.N. Adversarial Super-Resolution of Climatological Wind and Solar Data. *Proc. Natl. Acad. Sci. U. S. A.* **2020**, *117*, 16805–16815.

13.   Bárdossy, A. Introduction to Geostatistics. *Institute of Hydraulic Engineering, University of Stuttgart* **1997**.

14.   Yue, L.; Shen, H.; Li, J.; Yuan, Q.; Zhang, H.; Zhang, L. Image Super-Resolution: The Techniques, Applications, and Future. *Signal Processing* **2016**, *128*, 389–408.

15.   Ledig, C.; Theis, L.; Huszár, F.; Caballero, J.; Cunningham, A.; Acosta, A.; Aitken, A.; Tejani, A.; Totz, J.; Wang, Z.; et al. Photo-Realistic Single Image Super-Resolution Using a Generative Adversarial Network. In Proceedings of the Proceedings of the IEEE conference on computer vision and pattern recognition; 2017; pp. 4681–4690.

16.   Dong, C.; Loy, C.C.; He, K.; Tang, X. Image Super-Resolution Using Deep Convolutional Networks. *IEEE Trans. Pattern Anal. Mach. Intell.* **2016**, *38*, 295–307.

17.   Liebel, L.; Körner, M. Single-Image Super Resolution for Multispectral Remote Sensing Data Using Convolutional Neural Networks. *ISPRS-International Archives of the Photogrammetry, Remote Sensing and Spatial Information Sciences* **2016**, *41*, 883–890.

18.   Müller, M.U.; Ekhtiari, N.; Almeida, R.M.; Rieke, C. SUPER-RESOLUTION OF MULTISPECTRAL SATELLITE IMAGES USING CONVOLUTIONAL NEURAL NETWORKS. *ISPRS Annals of Photogrammetry, Remote Sensing and Spatial Information Sciences* 2020, *V-1-2020*, 33–40.

19.		Wang, Z.; Jiang, K.; Yi, P.; Han, Z.; He, Z. Ultra-Dense GAN for Satellite Imagery Super-Resolution. *Neurocomputing* **2020**, *398*, 328–337.

20.		G-PortalTop Available online: https://gportal.jaxa.jp/gpr/ (accessed on 14 June 2021).

21.		Armstrong, R.; Knowles, K.; Brodzik, M.; Hardman, M.A. DMSP SSM/I-SSMIS Pathfinder Daily EASE-Grid Brightness Temperatures. Version 2. *NASA National Snow Ice Data Center Distributed Active Archive Center: Boulder, CO, USA* **1994**.

22.		Remote Sensing Systems Available online: http://www.remss.com/support/crossing-times/ (accessed on 6 June 2021).

23.		Holmes, T.R.H.; De Jeu, R.A.M.; Owe, M.; Dolman, A.J. Land Surface Temperature from Ka Band (37 GHz) Passive Microwave Observations. *J. Geophys. Res.* **2009**, *114*, doi:10.1029/2008jd010257.

24.		Arlene Laing, J.-L.E. Ch. 2: Remote Sensing: 2.5 Satellite Detection of Clouds and Precipitation Available online: http://kejian1.cmatc.cn/vod/comet/tropical/textbook_2nd_edition/navmenu.php_tab_3_page_5.3.0.htm (accessed on 15 May 2021).

25.		Dai, L.; Che, T. Cross-Platform Calibration of SMMR, SSM/I and AMSR-E Passive Microwave Brightness Temperature. In Proceedings of the Sixth International Symposium on Digital Earth: Data Processing and Applications; International Society for Optics and Photonics, November 3 2010; Vol. 7841, p. 784103.

26.		Scott, K.A.; Andrea Scott, K.; Buehner, M.; Caya, A.; Carrieres, T. Direct Assimilation of AMSR-E Brightness Temperatures for Estimating Sea Ice Concentration. *Monthly Weather Review* 2012, *140*, 997–1013.

27.		He, K.; Zhang, X.; Ren, S.; Sun, J. Deep Residual Learning for Image Recognition. *2016 IEEE Conference on Computer Vision and Pattern Recognition (CVPR)* 2016.

28.		Ba, J.L.; Kiros, J.R.; Hinton, G.E. Layer Normalization. *arXiv [stat.ML]* 2016.

29.		Kingma, D.P.; Ba, J. Adam: A Method for Stochastic Optimization. *arXiv [cs.LG]* 2014.

30.		Long, D.G.; Brodzik, M.J.; Hardman, M. Enhanced-Resolution SMAP Soil Moisture Using Image Reconstruction. In Proceedings of the 2017 IEEE International Geoscience and Remote Sensing Symposium (IGARSS); July 2017; pp. 2499–2502.

31.		Long, D.G.; Brodzik, M.J. Optimum Image Formation for Spaceborne Microwave Radiometer Products. *IEEE Transactions on Geoscience and Remote Sensing* 2016, *54*, 2763–2779.

32.		Wang, Z.; Bovik, A.C.; Sheikh, H.R.; Simoncelli, E.P. Image Quality

16

Assessment: From Error Visibility to Structural Similarity. *IEEE Transactions on Image Processing* 2004, *13*, 600–612.

33.   Latham, J.; Cumani, R.; Rosati, I.; Bloise, M. Global Land Cover Share (GLC-SHARE) Database Beta-Release Version 1.0-2014. *FAO: Rome, Italy* **2014**.